Journal of Wind Engineering & Industrial Aerodynamics 195 (2019) 104000

Contents lists available at ScienceDirect

Journal of Wind Engineering & Industrial Aerodynamics

journal homepage: www.elsevier.com/locate/jweia

Effect of moving ground on the aerodynamics of a generic automotive model: The DrivAer-Estate

Shibo Wang [a,b,*], Terence Avadiar [a,b], Mark C. Thompson [a,b], David Burton [a,b]

[a] Monash Wind Tunnel Research Platform, Monash University, Australia
[b] Fluids Laboratory for Aeronautical and Industrial Research (FLAIR), Dept. of Mechanical Engineering, Monash University, Australia

ARTICLE INFO

Keywords:
DrivAer estate (station wagon)
Vehicle aerodynamics
Bluff body aerodynamics
Ground simulation
Computational fluid dynamics (CFD)
Detached Eddy simulation (DES)

ABSTRACT

With the recent trend to require automotive aerodynamic testing in wind tunnels with *rolling-road* floors, this study investigates the impacts of the ground configuration on the aerodynamic characteristics of a generic estate-type vehicle – the DrivAer-Estate. This is based on a comparison between time-dependent computational predictions for two configurations: one with a stationary ground with stationary wheels, and another with a moving ground and rotating wheels. This study quantifies the time-averaged flow structures, wake dynamics, surface pressure distributions and aerodynamic loadings, and by comparing these for the two cases. This study determines the distinct flow features and the mechanism of how different ground simulations affect the aerodynamic characteristics. Predictions using an Improved Delayed Detached Eddy Simulation (IDDES) model are validated where possible against time-mean wind-tunnel measurements, providing confidence in the simulation results. Indeed, the results show that due to the distinct flow features generated by estate-type geometries, the ground configuration only locally alters the flow field in close proximity to the ground, and therefore its impact on the flow near the automobile surfaces and in the wake is limited. Regarding the aerodynamic loadings, only the underbody surface pressure is found to be sensitive to the ground simulation, which leads to a variation in the lift coefficient by a factor of approximately two. However, the impact on the drag prediction is minimal, with the two drag coefficient predictions within 3% of each other, and consistent within the range of values from previous wind-tunnel tests.

1. Introduction

Automotive aerodynamics has witnessed remarkable development over the past decades, with extensive research and development contributing to improved fuel efficiency, reduced wind noise and better engine cooling, amongst other things.

The study of automotive aerodynamics in a wind tunnel changes the reference frame requires the use of a fixed vehicle with the fluid moving past. In contrast to the on-road use of vehicles which passes through the air and can be subject to environmental factors, this change of reference improves the ability to study the aerodynamic forces and wake characteristics. Automotive wind tunnel testing is undertaken with a vehicle fixed reference frame by moving the fluid over the vehicle. This reproduces the relative motion of the vehicle moving through the fluid, however it does not reproduce the relative motion of the vehicle and ground. As this is known to alter the aerodynamic behaviour of some vehicles, particularly those close to the ground (Hennig et al., 2011; Zhang et al., 2006), there has been a move to reproduce the relative motion by moving the ground plane in the wind tunnel, i.e., with a rolling road. Wind tunnel testing with a moving belt is now mandated by the Worldwide Harmonised Light Vehicles Test Procedure standards (WLTP) (Worldwide harmonized Ligh). However, the magnitude of the effect may differ depending on the car features (including wheels or afterbody features such as spoilers) and external geometry. Since the installation of a rolling road is a substantial and expensive undertaking, it seems worthwhile to try to quantify the expected modifications to the aerodynamics depending on automobile type.

Bearman et al. (1988) classified the wakes of automotive geometries into two modes: the longitudinal vortex mode and the quasi-axisymmetric recirculating mode. They further commented that ground effect is more pronounced on the former mode by showing a strong interference between the downwash induced by the vortex pair and ground motion. This is why they proposed that the effect of ground motion is sensitive to underbody structures, such as the rear upsweep

* Corresponding author. Monash Wind Tunnel Research Platform, Monash University, Australia.
E-mail address: shibo.wang@monash.edu (S. Wang).

https://doi.org/10.1016/j.jweia.2019.104000
Received 14 February 2019; Received in revised form 13 July 2019; Accepted 15 September 2019
Available online 15 October 2019
0167-6105/

angle (diffuser) and the ground clearance, as these features may interfere with the formation of wake longitudinal vortices. The effect of ground motion is more significant with a reduced ground clearance, as the momentum deficit caused by the presence of the ground boundary layer needs to be imposed in a more confined region. That is why accurately replicating the relative ground motion is likely to be more important for racing cars than passenger cars, as the generic ground clearance is much greater for road cars. Howell and Hickman, (1997), through studying the ground motion effect with a 1/4 scale car (the MIRA model), argued that for most aerodynamic development of passenger cars, using the fixed working section floor is adequate, but to acquire absolute results (e.g. drag measurements) a more accurate ground representation is essential.

According to a study on high-speed trains (Wang et al., 2018), two mechanisms are involved in how ground motion alters aerodynamic characteristics: (i) direct momentum deficit due to the boundary layer developed on the ground, and (ii) interaction between the boundary layer and wake developed around the vehicle. Because of these factors, ground motion significantly alters the characteristics of the underbody flow and wake, and hence affects integrated aerodynamic aspects, such as drag measurements. This impact is found to be more significant if the dominant wake structures are in proximity to the ground. For example, Wang et al. (2018) determined that high-speed train slipstream is sensitive to ground model, as the downwash flow pushes the wake trailing vortices towards the ground. Krajnović and Davidson, (2005) showed that the moving ground configuration can increase the mass flux underneath the vehicle in the streamwise direction, while decreasing it in the spanwise direction. Additionally, their study further concluded that the altered underflow is the cause of altered aerodynamic loading on the underbody structure. However, after reviewing studies with different geometries, a consistent trend was not established on the aerodynamic loading and flow. For example, Bearman et al., (1988) found that the ground movement reduced drag and lift by approximately 8% and 30%, respectively, and a similar trend was determined by Krajnović and Davidson, (2005) on a simplified fastback car showing a reduction of drag and lift at 8% and 16%, respectively. In contrast, according to tests on a simplified model (MIRA), Howell and Hickman, (1997) reported an increase in drag and a reduction in lift with the application of a moving belt, which was suggested to be due to an increased mass flow beneath the vehicle. Overall, the inconsistent trend of the ground simulation effect found for different automotive models suggests that the aerodynamic influence of the ground treatment is sensitive to car geometry. In addition, wheel rotation is another parameter that may have an influence. Generally, rotating and stationary wheels are coupled with moving and fixed ground configurations, respectively. Many studies (Bearman et al., 1988; Duncan et al., 2010; Guilmineau, 2014a) have shown the necessity of using rotating wheels with the moving ground configuration. For example, based on an investigation on isolated wheels, Bearman et al. (1988) determined that the vortex pair behind the wheel, which originates from the interaction of the wheel with the floor boundary layer, is stronger with a fixed wheel configuration.

For many years, reference automotive models have been widely used to understand the fundamental generic flow topology around an automobile and in the wake. Even though some studies have focused on specific car models, mainly for industry purposes, the majority of the studies have tended to adopt a generic or simplified car model for the following two reasons. First, the findings acquired from a generic model are more fundamental and universal, since they generally focus on the effect of a particular geometric aspect. Second, by utilising a generic benchmark model, researchers can more easily collaborate and communicate their findings, and together make further advancements. Given these benefits, reference car models are often utilised to investigate different aspects of automotive aerodynamics, like flow characterisation, ground simulation, drag reduction, flow control, acoustic performance, ventilation design, etc.

The most well-studied model is the *Ahmed body*, which was originally proposed by Ahmed et al. (1984). It utilises a heavily geometrically simplified model to replicate some of the bulk key flow features around a realistic car model – especially the rear end. In the initial study, Ahmed et al. (1984) identified the time-averaged wake structures, and studied their response to different base slant angles. Due to the simplicity of the Ahmed body, numerous studies have been conducted on it, extending knowledge of the effects of rear geometry on wake flow. Since the advent of Ahmed body, many studies of other reference models have been developed focusing on different geometry aspects; for example, the SAE reference model and the MIRA car model. Le Good and Garry, (2004) conducted a comprehensive review on applying reference models to automobile aerodynamics.

Studies of the wakes of simplified geometries, analogous to an estate vehicle, include those variants with a square-back or rear backlights with slant angles in excess of 30°, typically fully separated at the base. These models include the Ahmed et al., (1984), Windsor (Littlewood et al., 2011), ASMO (Aljure et al., 2014), and SAE (Cogotti, 1998) bodies. These models serve as good examples to elucidate the fundamental large-scale flow structures that are expected to be present for estate vehicles, for example, as elucidated by Avadiar et al. (2019) in reduced Reynolds number experiments. The recirculation lengths range between 0.33 and 0.37 vehicle lengths rearwards of the base, with the time-averaged recirculation vortex commonly represented as a toroidal structure (Volpe et al., 2014; Aljure et al., 2014). Duell and George (2000) identified two main wake frequencies, which they associated with shear layer vortex shedding and the longitudinal pumping of the free stagnation point, two mechanisms that are interdependent. Square-back geometries such as the Ahmed and Windsor model see a dominance of the left-right movement of the vortex structure of the wake torus, and exhibit long time-scale switching of the wake between a left and right bias, commonly referred to as the wake bi-stability. This feature was first thoroughly investigated by Grandemange on a bluff axisymmetric body (Grandemange et al., 2012) and an Ahmed squareback body (Grandemange et al., 2015), and was investigated further by Volpe et al. (2014) for the unsteady wake characteristics. Experiments on the square-back Windsor body by Pavia et al. (2018) considered the influence of wheels and body tapers on the suppression and sensitivity of this phenomenon, confirming that the presence of strong upwash or downwash would suppress the behaviour. Whilst the presence of bi-stability or overall symmetry breaking modes may exist for model geometries and even complex passenger vehicles (Bonnavion et al., 2017), the dominant time-averaged structure remains the most studied and related to principal forces acting on the vehicle.

However, due to extreme idealisation, distinct differences exist between the flow field generated by a traditional reference model (e.g. the Ahmed body) and a realistic vehicle, even though some qualitatively similarities exist. Therefore, it is dangerous to expect that knowledge acquired from simplified reference models can be applied naively to understand the aerodynamics of a production car. For example, important flow features identified on production cars, such as the shedding from the side mirrors, interaction between the A-pillar vortices and downstream wake structures, and the complex three-dimensional flow introduced by the highly curved rear end, are almost impossible to be investigated using a heavily simplified model. This limits the applicability of directly using a (highly simplified) reference model to understand the flow around a realistic car, and this was the motivation to introduce a more representative (more detailed) automotive reference model.

The DrivAer model was proposed by Heft et al. (2011) to bridge the gap between those heavily simplified models and production cars. The DrivAer is a blend of two representative production car models, the *Audi A4* and *BMW 3* Series. To achieve a high universality, DrivAer adopts a modular approach with three interchangeable rear geometries (i.e. fastback, estate and notchback) and two underbody configurations (i.e. detailed and smooth) (Heft et al., 2012a). Since this new benchmark model was launched in 2011, already many studies have been undertaken to quantify and analyse its aerodynamic performance. It has also

been commonly used as a reference model to calibrate experimental testing set-ups and to validate numerical codes.

More recently, Guilmineau (2014a) studied the ground motion effect on the DrivAer-Fastback model, and he found that the implementation of a moving ground and rotating wheels reduces the drag and lift. By comparing the performance of Reynolds-Averaged Navier-Stokes (RANS) and Detached Eddy Simulation (DES) models with experimental data, he proposed that the lift can only be accurately predicted by the DES approach with a more robust drag prediction (Guilmineau, 2014b). However, the wake behind a sedan/fastback type vehicle can be very different to the one developed behind an estate-type vehicle. For example, Avadiar et al. (2018) characterised the flow structures around the DrivAer-Estate, and found that the near-wake was dominated by the up-wash from underbody diffuser, instead of the downwash from the top surface as typically occurs for sedan/fastback vehicles.

The current study aims to advance our knowledge of ground simulation effects on estate-type vehicles, for which aerodynamic aspects are not well understood compared to classic sedan/fastback vehicles. Market sales of new automobiles has seen the decline of sedan/fastback vehicles, with continued strong sales of hatchbacks, SUVs and more recently, crossover variants that bridge SUV and estate geometry (Brewer, 2017). Therefore, it follows that the symptomatic fully separated wake of such vehicles be investigated. The DrivAer-Estate can be considered as a suitable geometry with a ground clearance similar to hatchbacks but less than SUVs, accentuating the influence of a changing ground boundary condition. Previous studies have shown that the influence of different ground simulations on the drag force experienced by the DrivAer-Estate is limited, compared with other DrivAer variants like fast-back. For example, the ground simulation reduces the drag of the fast-back by 4.3%, whereas the reduction on estate-back only shows 1.3% (Heft et al., 2012b). It is unclear whether the similarities observed in drag force are indicative of equivalent time-average and transient wake flows. This understanding is especially important for the application of fixed ground wind tunnels, and indeed, partial-belt moving ground wind tunnels, to investigations of wake flow control strategies, both active and passive. For example, it is known that the ground boundary layer, in the fixed ground case, will result in less underbody flow momentum than the moving ground case, but how this translates into wake effects is not well understood. The present study tries to answer these questions by mapping and explaining the effects of ground motion, or lack thereof, on the flow features in the wake. To fulfil this objective, two primary simulation cases based on: a stationary ground with stationary wheels (SG) and a moving ground with rotating wheels (MG), are performed and systematically analysed and compared.

2. Methodology

2.1. Car geometry and computational domain

The geometry utilised for this study is the *DrivAer-Estate* model, which is a generic car model proposed by Heft et al. (2011). The Computer-Aided Design (CAD) model of the DrivAer is available from the Technical University of Munich (Drivaer model,). Its length (L) to width (W) to height (H) ratio is approximately 4.61 : 2.03: 1.42; the width inclusive of the side mirrors. The underbody configuration used in this study was the smooth floor, consistent with earlier work and of a similar configuration to work by Ashton and Revell, (2015) and Collin et al. (2016). As the DrivAer geometry configurations include a flat underbody, this configuration was chosen at the start of these series of studies to simplify the sources of turbulent flow structures within the wake of the vehicle. The strength and convection of these flow structures will likely be different between the two underbody configurations owing to the high degree of upwash in the wake from the underbody exit flow. However, the emphasis remains on the wake flow structures that contribute the most towards the drag. We also expect that in the case of a "rough" underbody there will be an increase in underbody losses for the MG case, as there is greater underbody momentum, at some point resulting in an increase in overall drag. So, it is interesting that there is a sensitivity to underbody roughness and there is a relative drag reduction for the MG smooth underbody, and one that is consistent with the experimental results of Heft et al. (2012b). Further, the general trend in automotive design is towards a flat underbody. This is likely to be more so with increased electrical vehicles in the market. Note that the vehicle width presented in this paper includes the side mirrors. Compared with the original physical model, some minor geometric alterations are applied to optimise the geometry for undertaking numerical simulations. For example, the wheels are covered with flat surfaces, i.e., the wheel rims are not modelled. As this study focuses on external aerodynamics, the ventilation system is not simulated with the intake panels, which are instead modelled as closed surfaces. The contact patch between the wheels and ground is modelled by a rectangular section, extruded with a dimension of 200 × 200 mm (width × length) as illustrated in Fig. 1 (c). This is to maintain a good quality mesh near the contact zone. Schematics of the car model are presented in close-up views in Fig. 1.

The car is positioned in the centre of a hexahedral computational domain, and the boundary arrangement is illustrated in Fig. 1. The origin of the coordinate system is positioned in the spanwise mid-plane at the ground height, with $x = 0$ corresponding to the rear end of the car. The size (length: width: height) of the computational domain is $19.5H : 11.4H : 6H$, which is equivalent to $6L : 8W : 6H$. This gives a blockage ratio of 0.015. The low blockage ratio is chosen to replicate the vehicle travelling in an open-air environment; in other words, to

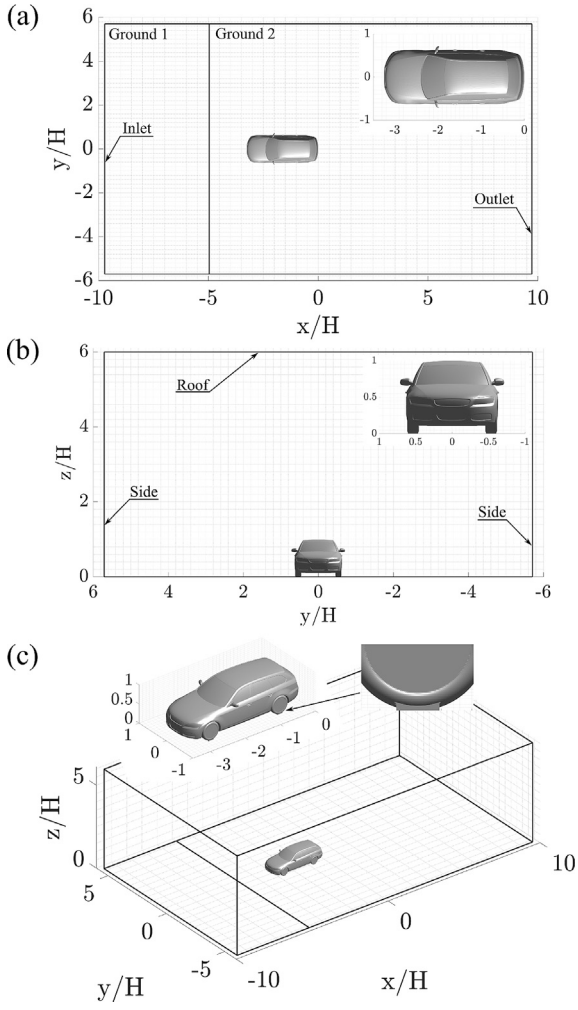

Fig. 1. Schematics of the car geometry and computational domain: (a) top-view; (b) front-view, (c) isometric-view.

ensure the blockage is negligible. Additionally, the inlet and outlet are placed 2L and 3L in front of and behind the car, to provide sufficient space for the incoming flow to establish before it approaches the car and to allow the wake be reasonably fully developed. While larger inflow and outflow lengths are desirable, the choice reflects a compromise to restrict computational resource requirements.

2.2. Boundary conditions

To determine the effects of the ground motion condition, two cases are studied: SG and MG. The two cases have the same geometries with the only difference being the boundary conditions of the wheels and ground surfaces. The predictions of this study are compared to measurements from wind-tunnel experiments (Avadiar et al., 2018) undertaken at Monash University for validation purposes. Therefore, in order to replicate the floor configuration in the experimental set-up, where a rolling road is not available, the ground is divided into two parts identified as *Ground 1* and *Ground 2*, as illustrated in Fig. 1.

The SG case is designed to replicate the wind-tunnel set-up; the distance between the leading edge of Ground 2 and the car model in the numerical simulation is equivalent to the distance between the open jet nozzle exit and the car in the wind-tunnel. The (no-slip) stationary ground condition is applied to Ground 2 to simulate a fixed wind-tunnel floor, while a zero-shear (slip) condition is applied to Ground 1 to avoid ground boundary layer development prior to Ground 2. Additionally, a no-slip wall condition is applied to the wheels for consistency in this case.

The MG case represents the realistic condition of a car travelling through still air where there is no relative motion between the ambient air and the ground. In the MG configuration, both Ground 1 and 2 employ a no-slip moving wall condition with a uniform freestream velocity. Rotational wheels are coupled with the moving ground, for a realistic representation. In this study, the wheels rotate at a constant angular velocity, with the speed at the tyre radius equal to the speed of the moving ground. Based on a comparison of surface pressure between applying an angular velocity boundary condition and adopting true rotating wheels on a production hatchback vehicle, Duncan et al. (2010) reported that the discrepancies between the two approaches are insignificant. The boundary conditions of the ground surfaces and wheels for each case are summarised in Table 1.

Apart from the wheels and ground surfaces, the conditions for other boundaries are identical. A uniform velocity boundary condition with a turbulence intensity of 1% is applied at the inlet. The Reynolds number (based on car length L) is 8×10^6. This value is set to match the wind-tunnel experimental condition for consistency, and corresponds to the vehicle travelling at 100 km/h (Avadiar et al., 2018). A zero static pressure condition is applied at the outlet boundary. Symmetry boundary conditions are applied to far-field planes, for example the sides and top of the computational domain. All car surfaces, other than the wheels in the MG case, adopt stationary no-slip wall boundary conditions.

2.3. Solver description

The simulations in this study were undertaken with the commercial CFD code FLUENT, which is part of the ANSYS (16.2) software suite. In order to capture the highly turbulent and presumably incompressible flow, the pressure-based transient solver was adopted.

The overall simulation procedure is summarised here. To start with, the velocity and pressure on the computational domain were initialised from a second-order steady-state Reynolds-Averaged Navier-Stokes (RANS) simulation. The turbulence model selected for the initial RANS simulation was the Shear-Stress Transport (SST) $k-\omega$ model, due to its superior performance modelling the near-wall boundary layer regions with undefined separation points. Subsequently, the Improved-Delayed Detached Eddy Simulation (IDDES) turbulence model was utilised to capture the transient features of the flow. The IDDES model was developed based on the classic Detached Eddy Simulation (DES) turbulence model, but improves accuracy within the RANS-LES blending region by applying an *improved delayed shielding function*. This also improves the wall-modelling capability. The SST $k-\omega$ model was applied for the RANS regions within IDDES to capture boundary layer development. The multi-scale turbulent structures away from the wall boundaries, i.e., vortical wake structures, are resolved by the LES model within IDDES. A more detailed description of the IDDES model is presented in the FLUENT User's Guide (Fluent) and literature references therein.

A time-step of $0.0035T_{ref}$ was chosen for the CFD solver to restrict that the flow only convects one cell per time-step within the refinement regions, i.e., the Courant number ≤ 1 for the typical smallest cells, according to the guidelines for conducting IDDES simulations. Here, $T_{ref} = H/U_\infty$ is a reference time scale that is defined as the time of a fluid parcel to travel one vehicle height at the freestream velocity. For the spatial discretisation, the second-order upwind scheme was applied to the convective terms in the turbulence equations, while the bounded central differencing scheme was used for the momentum equations, given the high Reynolds number involved. Additionally, the bounded second-order implicit formulation was used for time-advancement of the transient momentum equations. Time-averaged statistics were recorded after the flow field reached an asymptotic state, which was checked through comparisons with predictions based on smaller averaging periods. Time-averaged statistics were taken over $202.8T_{ref}$, which is equivalent to 62 times the time taken for the freestream flow to advect the car length. The computational time for each simulation is approximately 50 KCPU hours.

Table 1
Boundary conditions of the ground surfaces and wheels.

	Ground 1	Ground 2	Wheels
SG	Zero-shear stationary wall	No-slip stationary wall	No-slip stationary wall
MG	No-slip moving wall	No-slip moving wall	No-slip rotational wall

2.4. Meshing strategy

The overall meshing strategy adopted in this study is the predominantly Cartesian hexahedral approach with substantial local refinements around the car and in the wake, as illustrated in Fig. 2.

A relatively smooth transition is applied to avoid sudden cell size changes across refinements zones, while noting that the cut-cell approach means that the cell resolution drops by a factor of two across zone boundaries. The different resolution zones are sized to ensure the local scales of flow structures are comfortably resolved across boundaries. The final zoning was developed over several iterations of mesh development. Additionally, prism-layer cells are applied to all wall boundaries to capture the boundary layer development, and a smooth transition is established between the outer inflation layer and the hexahedral grid.

To verify mesh independence, three meshes are examined, designated as the coarse (only applied to the SG case), medium and fine mesh. They are constructed based on the identical meshing strategy but with different local resolutions. Relative to the coarse mesh, the medium mesh was created by halving the car surface and surrounding cell size, and increasing the number of inflation layers by 2. Same approach was applied to construct the fine mesh based on the medium mesh. By doing this, the cell count increases from 3 million for the coarse grid to 31.9 million for the fine grid. The detailed meshing parameters are listed in Table 2.

Mesh independence is examined based on the velocity ($\overline{U}/U_\infty$) profiles at 0.5 to 1H behind the car, as illustrated in Fig. 3. Based on the prediction of the wake flow field at these positions, the difference between the different mesh predictions are small for both ground configurations. The main difference occurs within 0.25H of the ground, where the finer grid gives a slightly better prediction at both downstream locations. As a Scale-Resolving Simulation, further refining the mesh and

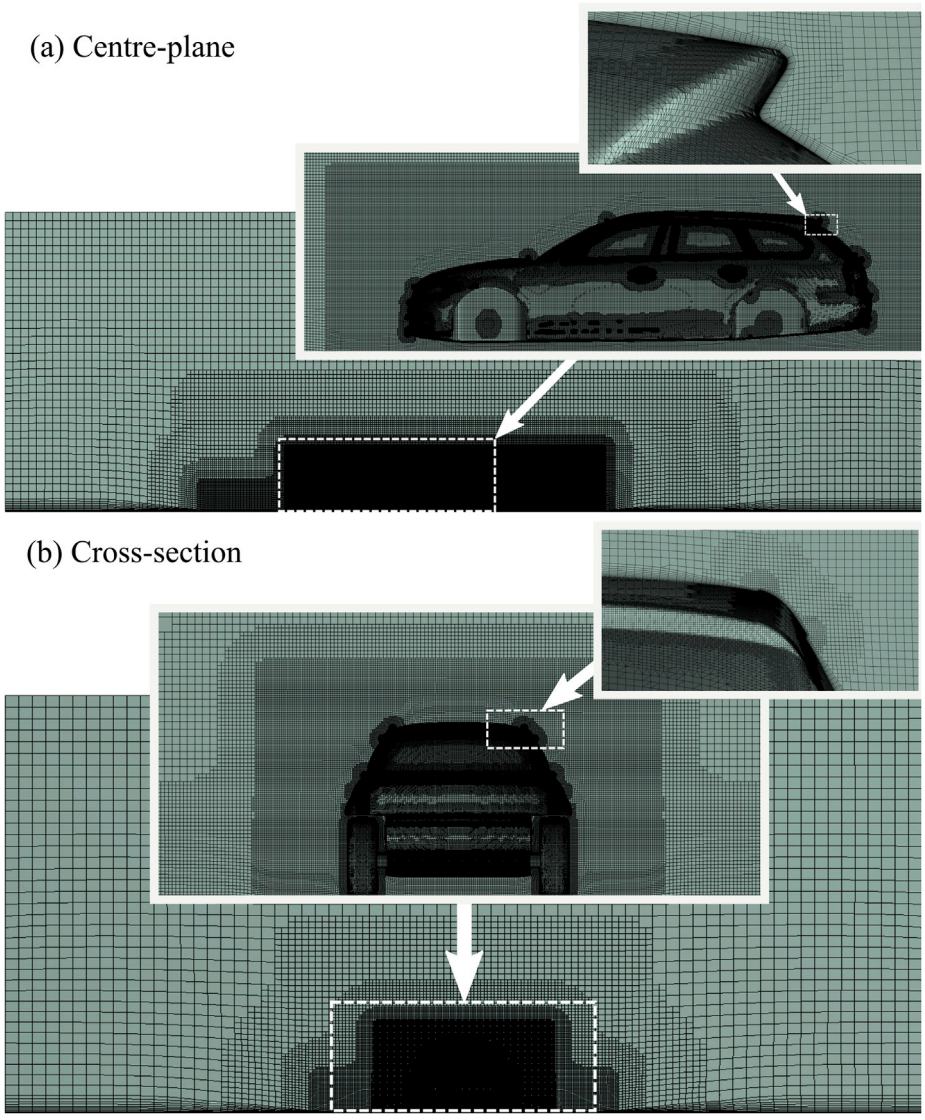

Fig. 2. Illustration of the mesh refinement regions around the car based on the fine mesh: (a) centre-plane; (b) cross-section.

Table 2
Key meshing parameters.

	Coarse	Medium	Fine
Car surface & surrounding cells	0.01H ~ 0.02H	0.005H ~ 0.02H	0.005H ~ 0.01H
Refinement zones	0.08H – 0.32H	0.04H ~ 0.16H	0.04H ~ 0.16H
Number of inflation layers	6	8	10
Car surface wall y^+	20–150	5–60	2–40
Number of cells (millions)	3.0	9.3	31.8

correspondingly reducing the time step can resolve more smaller eddies. However, given the fit between the predictions and experimental measurements, and noting the computational expense associated with further increasing mesh resolution, the resolution of the fine grid was regarded as sufficient, and all results presented in this paper are based on the fine mesh.

2.5. Validation

To validate the numerical methods and solver settings, the CFD predictions were compared with the wind-tunnel (WT) experimental measurements. The wind-tunnel experiment was conducted in the Monash University 1.4 MW closed-circuit wind-tunnel, and a full description of the experimental set-up and results are provided in the companion experimental study (Avadiar et al., 2018). In the current study, validation is undertaken against important aerodynamic measures such as velocity profiles (Fig. 7), wake topology (Figs. 9 and 10), surface pressure (Fig. 17) and aerodynamic loading (Table 3); with the comparisons showing relatively good agreement. The numerical simulations show a high accuracy in resolving the flow field, for example the prediction of the wake velocity profiles and the core position of the trailing vortices. Some minor discrepancies between the CFD and WT results might be attributable to deficiencies in both the numerical and the experimental modelling. Numerically, geometric simplification of the car model and turbulence modelling inadequacies can potentially introduce uncertainties/inaccuracies. Limitations are also present in wind-tunnel experiments; for example, the inability to measure reverse flow with the four-hole dynamic pressure probe (TFI cobra probe) and the presence of a streamwise pressure gradient. Despite these factors, as discussed further below, the overall agreement between measurements and predictions is good.

3. Results and analysis

This section starts with a description of the flow field around the car,

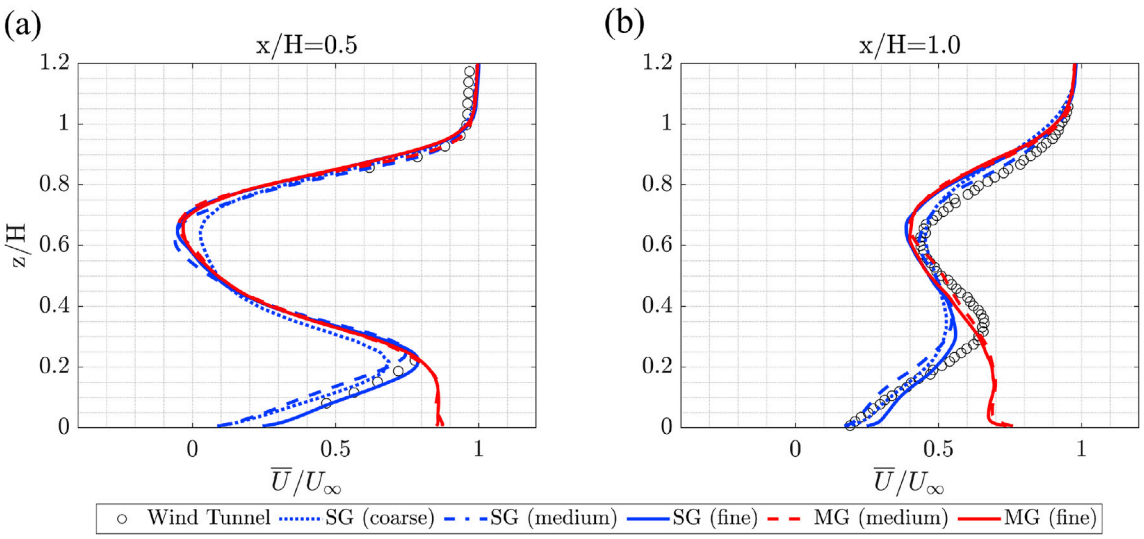

Fig. 3. Mesh independence test based on the velocity profiles ($\overline{U}/U_\infty$) at (a) $x/H = 0.5$, and (b) $x/H = 1$.

Table 3
The comparison of aerodynamic loadings between the SG and MG cases.

	C_D		C_L	
	Mean	Standard deviation	Mean	Standard deviation
SG	0.307	0.0080	−0.123	0.0371
MG	0.298	0.0077	−0.221	0.0369

and then considers the influences of the different ground boundary conditions. For a comprehensive understanding of the flow field, both time-averaged and dynamic flow features are presented and analysed. After that, the resultant impact on the car surface pressure due to the altered flow is determined. Finally, the force component predictions are presented for the two cases and compared with experiments and previous studies.

3.1. Flow characterisation around the car

To fully quantify the flow structure around the car, predictions at multiple locations are recorded and analysed. These locations are illustrated in Fig. 4. They consist of the spanwise centre-plane (coloured in red), two horizontal planes at $z/H = 0.3$ and 0.5 (coloured in blue), and three vertical planes at $x/H = 0.5$, 1 and 2 (coloured in green). These planes cover the critical representative regions around the vehicle, especially the wake region. In this study, flow quantities, e.g., the velocity and vorticity components, at these locations are exported and sampled every 10 time-steps, which is equivalent to the data acquisition time-step of $0.035T_{ref}$. For reference, at a vehicle speed of 100 km/h, this is equivalent to a frequency of 560 Hz, which essentially represents the highest cut-off frequency in the spectrum analysis.

3.1.1. Analysis of time-averaged statistics

To start with, iso-surfaces of positive mean Q-criterion of 0.1 s^{-2} are used to extract the coherent time-mean vortical structures around the car, as illustrated in Fig. 5. The iso-surfaces are coloured by time-averaged longitudinal vorticity ($\overline{\omega_x}$). According to Fig. 5, SG and MG demonstrate a qualitatively similar flow structure, except that in the SG case, a horseshoe-type vortex is generated in front of the car and more small-scale structures are produced on the stationary ground. Clearly, the ground motion locally alters the flow field in proximity to the ground, with minimal effect of the flow field around the rest of the car.

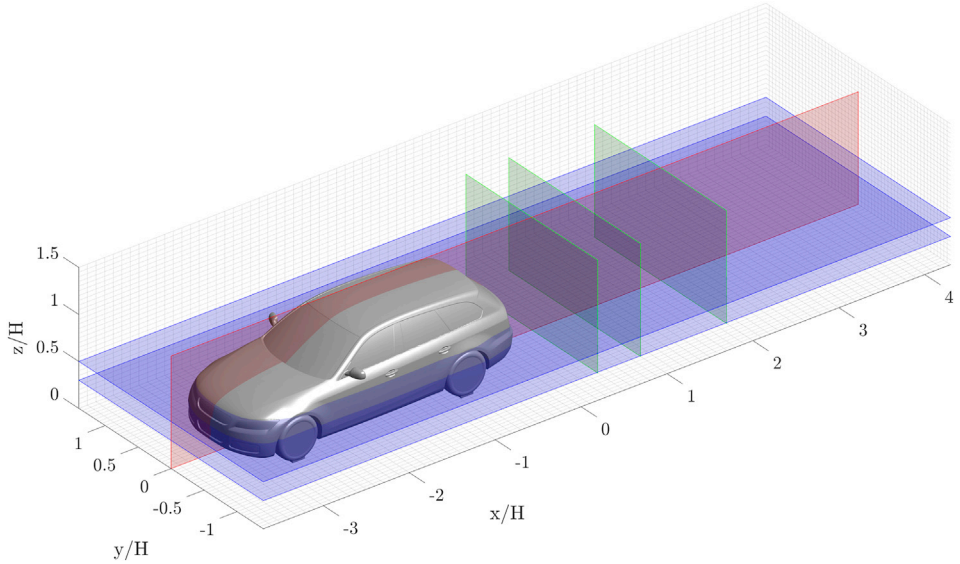

Fig. 4. The illustration of the location of planes where the flow data is collected.

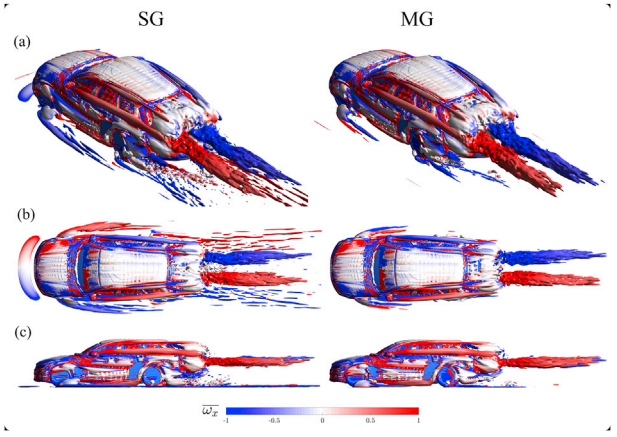

Fig. 5. DIfferent views comparing the coherent structures around the car for the two cases visualised by the mean Q-criterion iso-surface of 0.1 s^{-2} and coloured by $\overline{\omega_x}$. (For interpretation of the references to colour in this figure legend, the reader is referred to the web version of this article.)

Fig. 5 illustrates that vortical structures with various scales are developed around the car; for example, the A-pillar vortices, the vortices developed around the wheels and side mirrors, and the large wake structures. The wake is formed by multi-scale vortical structures peeling off at the back of the car. Additionally, Fig. 5 implies that the vortices generated upstream, for example the A-pillar vortices and the vortices developed around the side mirrors, feed into and interact with larger-scale wake structures. After mixing and interacting in the near wake, a dominant wake structure consisting of a counter-rotating longitudinal vortex pair is formed. The propagation of trailing vortices emanating from the base can be interpreted from the velocity and pressure at consecutive planes in the wake based on the numerical work conducted by Soares et al. (2017). Additionally, the existence of a pair of trailing vortices was also determined from the wind tunnel testing (Avadiar et al., 2018). Unlike the typical downwash vortices peeling off from the back of ground vehicles, observed for fast-back cars and high-speed trains, this vortex pair forms downstream of the car base surface. The formation, propagation and dynamic responses will be discussed in the following sections. Other structures like the horseshoe-type vortices created at the corner of the hood and windscreen, and the vortices created due to the flow separation around the wheels and at the back of the car are also captured in Fig. 5.

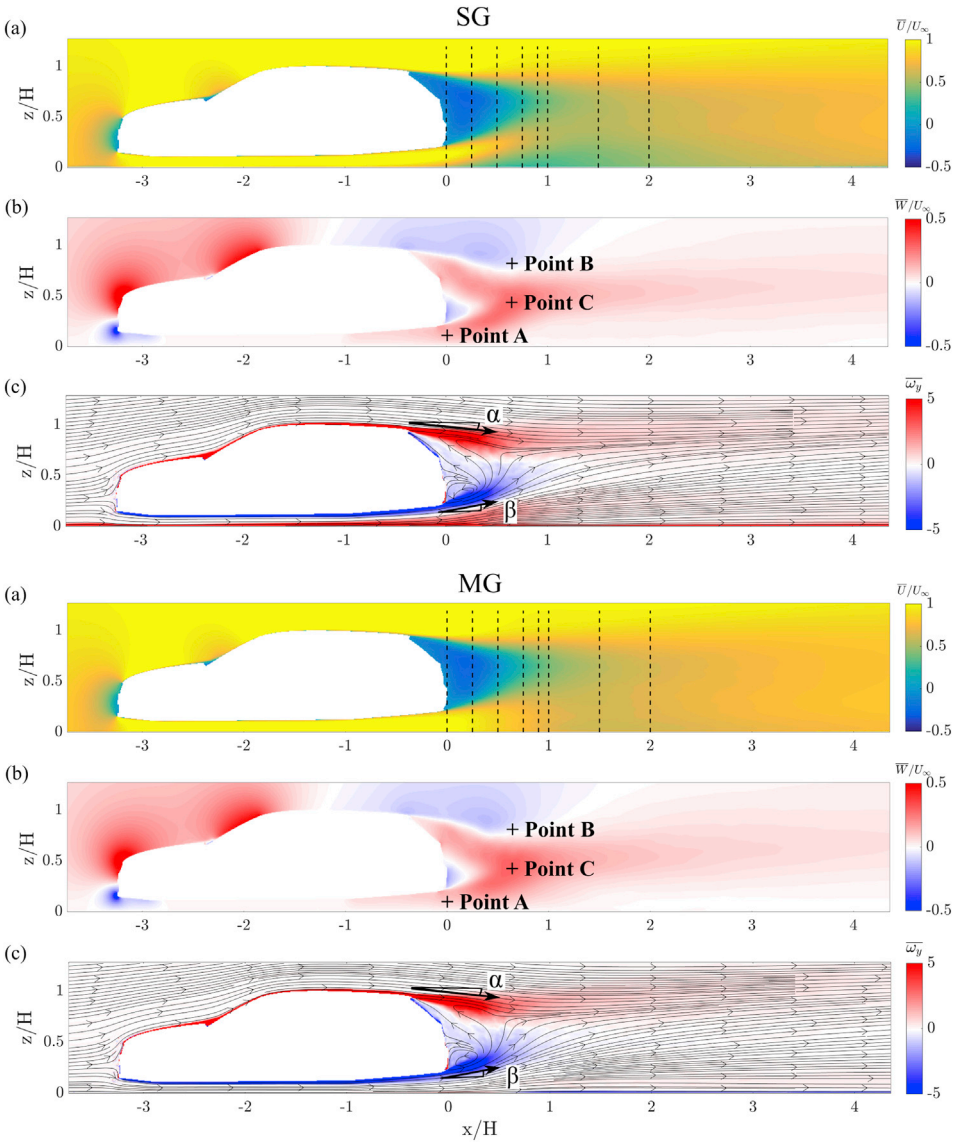

Fig. 6. The comparison of the flow field at the centreplane ($y/H = 0$): (a) $\overline{U}/U_\infty$; (b) $\overline{W}/U_\infty$; (c) $\overline{\omega_y}$ and in-surface projected velocity streamlines.

The impact of the ground motion can be clearly identified from the flow field at the spanwise centreplane ($y/H = 0$). In this study, the time-averaged flow field on the centreplane is quantified by the normalised x-velocity ($\overline{U}/U_\infty$), z-velocity ($\overline{W}/U_\infty$) and resultant y-vorticity ($\overline{\omega_y}$), as presented in Fig. 6. Additionally, in-surface projected velocity streamlines are plotted over the $\overline{\omega_y}$ contours to visualise the flow patterns. The comparison between Fig. 6 (a) and (b) illustrates that $\overline{U}/\ U_\infty$ is more affected by ground motion than $\overline{W}/U_\infty$, especially at lower heights. The stationary ground encumbers the underbody flow, and creates a low-speed flow region behind the diffuser. With respect to vorticity, the stationary ground introduces a persistent thin positive $\overline{\omega_y}$ region above the ground due to the relative motion between the ground and fluid. By comparing the streamlines and the flow pitch angle at the top and the bottom of the car, the effect of the ground motion on the recirculation region is not significant. For example, Fig. 6 shows that the pitch angles of the downwash and upwash from the spoiler (α) and diffuser (β) are relatively small, which are approximately 5.4° & 9.3° for the SG case, and 5.7° & 7.5° for the MG case respectively. This is expected due to the relatively large ground clearance of DrivAer-Estate, which makes the jet flow, from the diffuser, less ground motion dependent.

For a more quantitative comparison, the $\overline{U}/U_\infty$ p$x/\ H = 0$ rofiles from to 2 are plotted in Fig. 7. In addition, wind-tunnel measurements are also provided for validation purposes. The locations at which the velocity profiles are provided are visualised by the dashed lines in Fig. 6(a). Consistent with the contours in Figs. 6 and 7 shows that the discrepancy between the experimental SG case and numerical MG case caused by the different ground motion is more pronounced at a lower height. Additionally, the vertical extent of the discrepancy region expands as the flow propagates downstream due to the growth of the ground boundary layer. For example, the affected region increases from approximately 0.1 vehicle heights at the rear of the car to 0.6 vehicle heights at $x/H = 2$. Beyond the ground boundary layer region, the difference between the SG and MG profiles is almost negligible. The negative x-velocity captured between $x/H = 0$ and 0.5 corresponds to the mean flow recirculation region behind the car, where this region is clearly indicated by the streamlines in Fig. 6 (c). Once again, the experimental data was measured by four-holed Cobra probes, which are not capable of capturing this reversed flow (Avadiar et al., 2018). A good agreement is established between the numerical simulation (i.e. the SG case) and measurements.

Additionally, the time-averaged flow-field at two heights: $z/H = 0.3$ and 0.5, are analysed and compared. Similar to the comparison at the centreplane, the normalised x-velocity ($\overline{U}/U_\infty$), y-velocity ($\overline{V}/U_\infty$) and the corresponding z-vorticity ($\overline{\omega_z}$) are plotted in Fig. 8. In addition, the in-surface projected velocity streamlines on the two horizontal planes are provided. According to Fig. 8, the boundary layer that develops on the stationary ground reduces the local flow velocity in both the streamwise and spanwise direction, which results in a wider wake behind the car, and this influence is more pronounced at lower heights. In terms of vorticity, the shedding from the rear wheels, which is captured by the high $\overline{\omega_z}$ region, is more concentrated with the absence of the ground boundary layer.

Furthermore, the ground motion effect on the propagation of the time-averaged wake structure is studied based on the results at three sequential planes between $x/H = 0.5$ and 2, where the locations are illustrated in Fig. 4. The downstream wake evolution is depicted by the streamwise vorticity ($\overline{\omega_x}$) and in-surface projected velocity vectors in

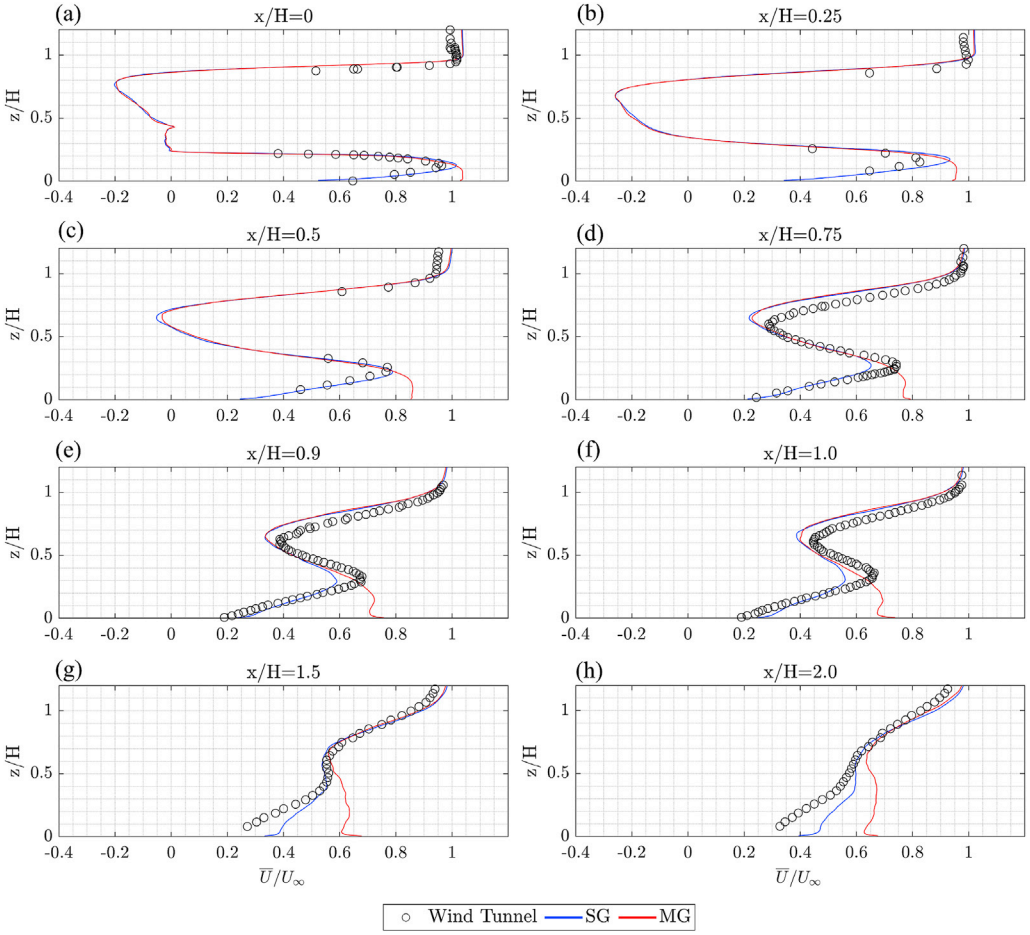

Fig. 7. The comparison of the centreline $\overline{U}/U_\infty$ profiles at: (a) $x/H = 0$; (b) $x/H = 0.25$; (c) $x/H = 0.5$; (d) $x/H = 0.75$; (e) $x/H = 0.9$; (f) $x/\ H = 1$; (g) $x/\ H = 1.5$; (h) $x/H = 2$.

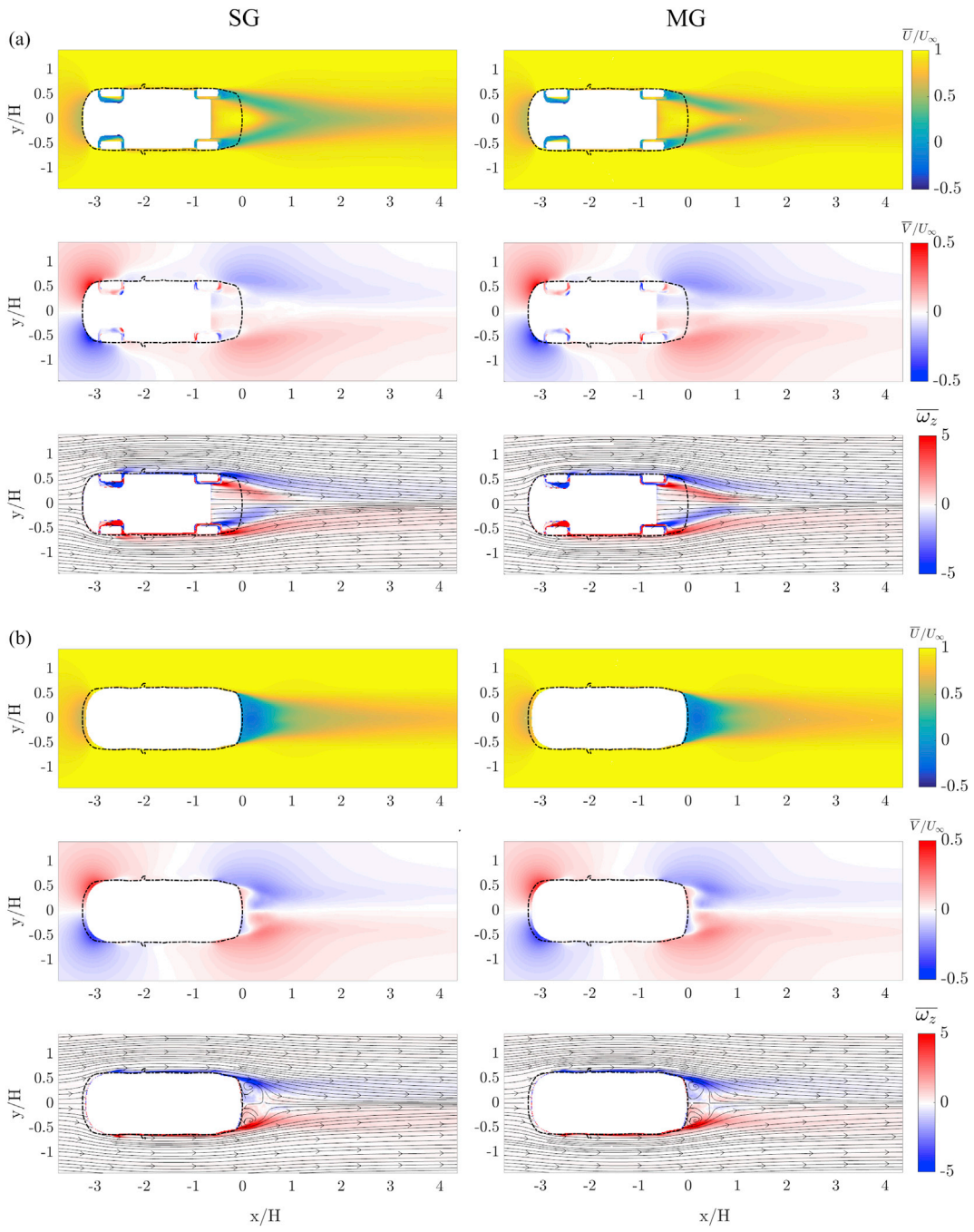

Fig. 8. The comparison of $\overline{U}/U_\infty$, $\overline{V}/U_\infty$, $\overline{\omega_z}$ and in-surface projected velocity streamlines at: (a) $z/H = 0.3$; (b) $z/H = 0.5$.

Fig. 9, and streamwise turbulence intensity (I_{uu}) in Fig. 10. In addition, the boundary of the vortical regions is defined by the iso-line of $\Gamma_2 = 2/\pi$ with the core identified by the local maximum of Γ_1; these provide commonly used vortex identification measures (Graftieaux et al., 2001). The wind-tunnel results are also presented in Figs. 9 and 10 for validation, noting again that a good agreement is established between the experimental and numerical results. Due to the limitation on capturing the reversed flow in the wind-tunnel tests, the recirculation region at $x/H = 0.5$ is not expected to be accurately resolved experimentally.

The three sequential planes between $x/H = 0.5$ and 2 are utilised to reveal the flow characteristics in the near and intermediate wake. At $x/H = 0.5$, apart from the dominant twin streamwise vortices, multiple flow structures with different scales are also captured in the near-wake region, including the pillar vortices, and shedding from the side mirrors and wheels. The interaction between these multi-scale structures is associated with the high turbulence region at approximately $z/H = 0.5$, as illustrated in Fig. 10 (a). Starting from $x/H = 1$, the streamwise vortex pair is more easily identified after the interaction and merging of multi-scale near-wake structures. By comparing the vortex boundary and core location between $x/H = 1$ and 2, the vortex pair propagates horizontally without significant influence of either downwash from the roof or upwash from the diffuser. Additionally, the downstream propagation of the streamwise vortex pair is not significantly influenced by ground motion both in terms of size and location. This is primarily because the ground motion only imposes a local effect through the ground boundary layer in proximity to the ground, while the vortex pair propagates above that region. Importantly, although this wake vortex pair is superficially similar to the rear pillar vortices found behind sedan/fastback vehicles or

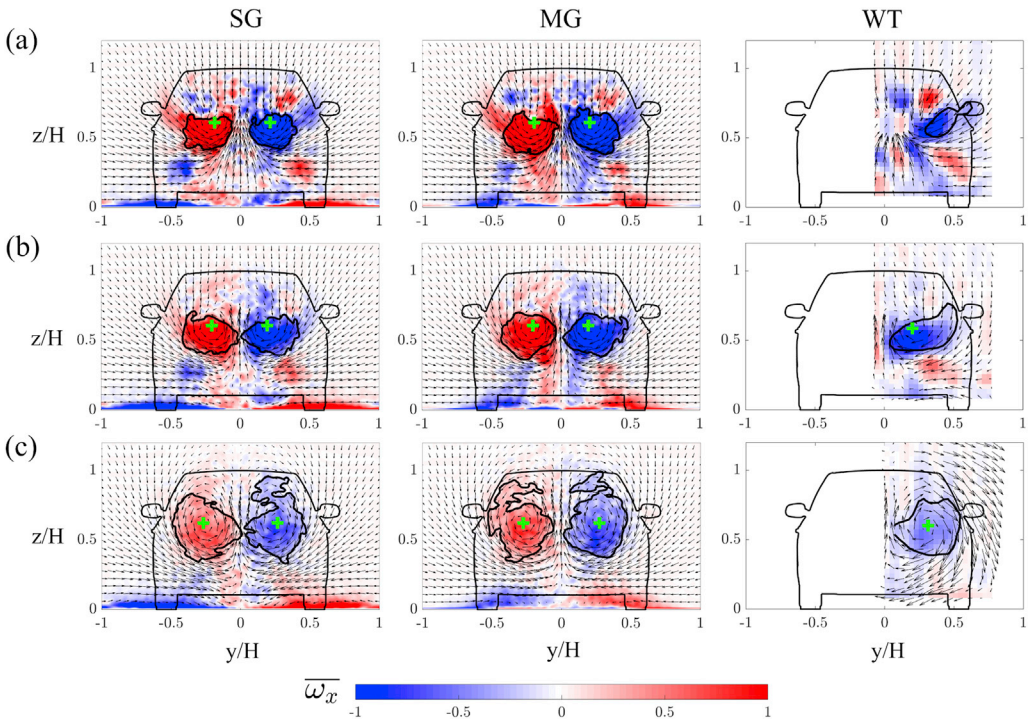

Fig. 9. The comparison of wake propagation based on $\overline{\omega_x}$ and in-surface projected velocity vectors at: (a) $x/H = 0.5$; (b) $x/H = 1$; (c) $x/H = 2$. The boundary of the vortices (shown by the black solid line) are determined by the iso-line of $\Gamma_2 = 2/\pi$, and the vortex cores (highlighted by the green "+") are identified using local maximum values of Γ_1. For location referencing, the boundary of the car is plotted with a black solid line. (For interpretation of the references to colour in this figure legend, the reader is referred to the Web version of this article.)

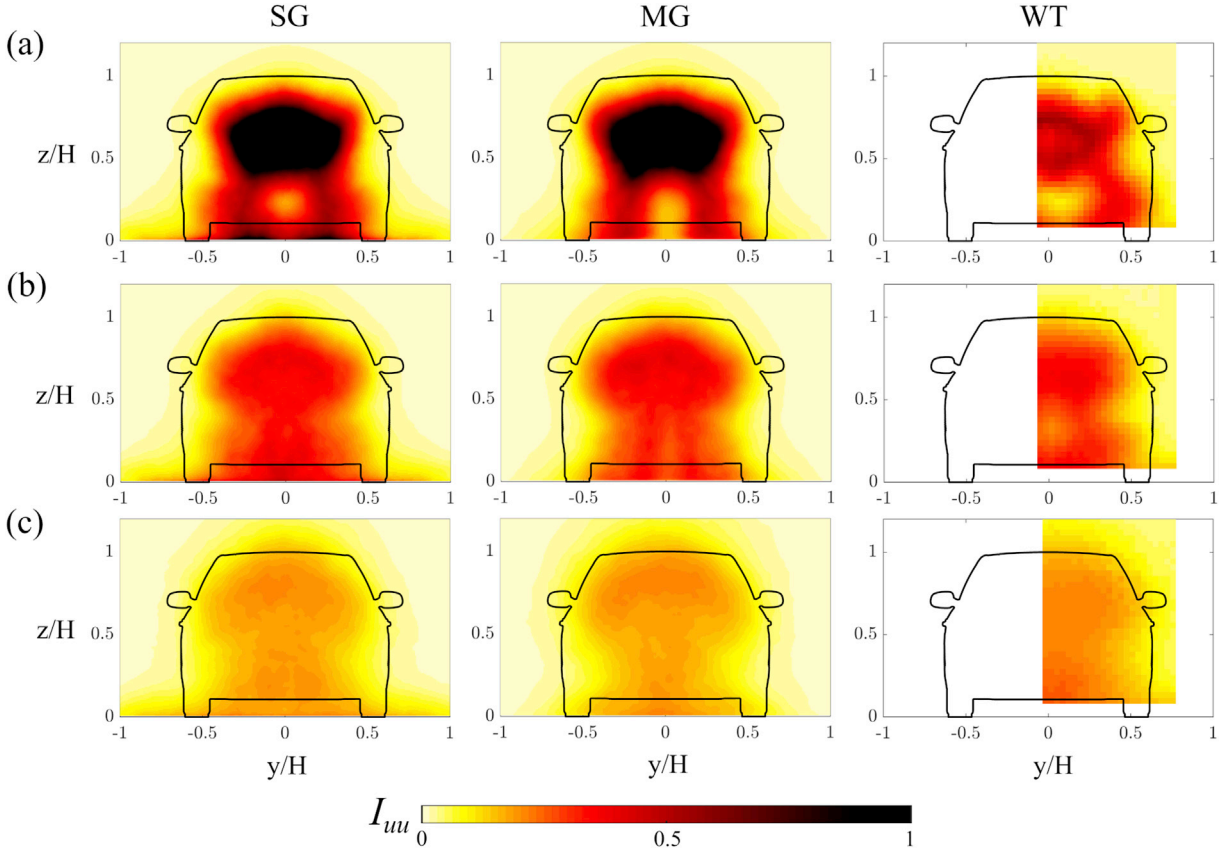

Fig. 10. The comparison of wake propagation based on normalised streamwise turbulence intensity (I_{uu}) at: (a) $x/H = 0.5$; (b) $x/H = 1$; (c) $x/H = 2$. For location referencing, the boundary of the car is plotted with a black solid line.

trailing vortices behind high-speed trains, inherently it is very different. The longitudinal vortices from the rear pillar or behind a high-speed train result from boundary layer vorticity peeling off from the edge of the surface and tilting downstream. However, the vortex pair behind the DrivAer-Estate is formed away from the base surface as a result of the interaction between multiple wake features.

3.1.2. Transient flow characteristics

As determined in *Section* 3.1.1, the time-averaged wake structure is highly 3-dimensional and turbulent, and this section focuses on the wake dynamic behaviour subject to the different ground simulations.

To start with, the ground simulation effect on the spanwise vortex shedding from the top and bottom of the vehicle is investigated. This analysis is implemented based on three points (Point A, B and C) within the vertical centreplane, where the locations are identified in Fig. 6(b). These points are assigned to capture the dynamic response of the jet flow from the diffuser (Point A), and shedding from the top (Point B) and bottom (Point C) of the car.

The coordinates (x-coordinate, z-coordinate) of point A, B and C are ($0H$, $0.12H$), ($0.6H$, $0.8H$) and ($0.6H$, $0.4H$), respectively. The power spectral densities (PSD) of the u-, v-, w-velocities at each point are presented in Fig. 11. In this study, the shedding frequency is quantified by the Strouhal number ($St = f\sqrt{A}/U_\infty$) based on the square root of the vehicle frontal area ($\sqrt{A}$, with f the shedding frequency). The changing of reference length scale here is to be consistent with wind tunnel experiment, and the underlying reason is that $sqrt(A)$ would be more representative of the effective wake size, rather than simply looking at 2D plane data, where H may be more relevant. The signal is split into segments of 42.25 T_{ref} long, which is equivalent to the length of 8 shedding cycles at the dominant frequency of $St = 0.2$ measured in the wind-tunnel. The overall spectra is averaged over these fast Fourier transform segments, 6.4 segments in total based on the specified segment length, with Hanning windows with 25% overlap. The variance (Var) of each signal is also provided in Fig. 11. According to Fig. 11, both SG and MG show generally broad spectra without strong spectral peaks, although there is considerable energy in frequency components in the range $St \leq 1$ in several of the spectra. This implies that the near-wake structure is chaotic and consists of a wide range of turbulent scales, instead of being dominated by distinct quasi-periodic dynamic features. Comparing the spectra between the three points, it can be seen that the differences between the SG and MG cases are more identifiable at a lower height (i.e., point A and C), which is consistent to the unsteady statistical results presented in *Section* 3.1.1.

Additionally, to investigate the relationship between the top and bottom spanwise shedding and how it alters with ground motion, cross-correlations of the streamwise (u) and vertical (w) velocity between every two points are implemented, and the results are plotted in Fig. 12. The time lag is normalised with T_{ref}. According to Fig. 12, there is no clear correlation between point A and B, which implies that the underbody flow and shedding from the spoiler are largely independent. Not surprisingly, a strong correlation is identifiable between the streamwise velocity at point A and C with a time delay of approximately 0.5 T_{ref}, as the underneath jet flow convects downstream. In comparison, for both cases, the correlation in the vertical direction is not as strong. The MG case indicates a weak dependency in the z-velocity, but the presence of ground boundary layer erodes this dependency. The wake response in the vertical direction is revealed by the correlation between the shedding from the top (represented by point B) and bottom (represented by point C). An out-of-phase correlation in the streamwise direction and in-phase correlation in vertical direction signifies the vertical oscillation of the wake.

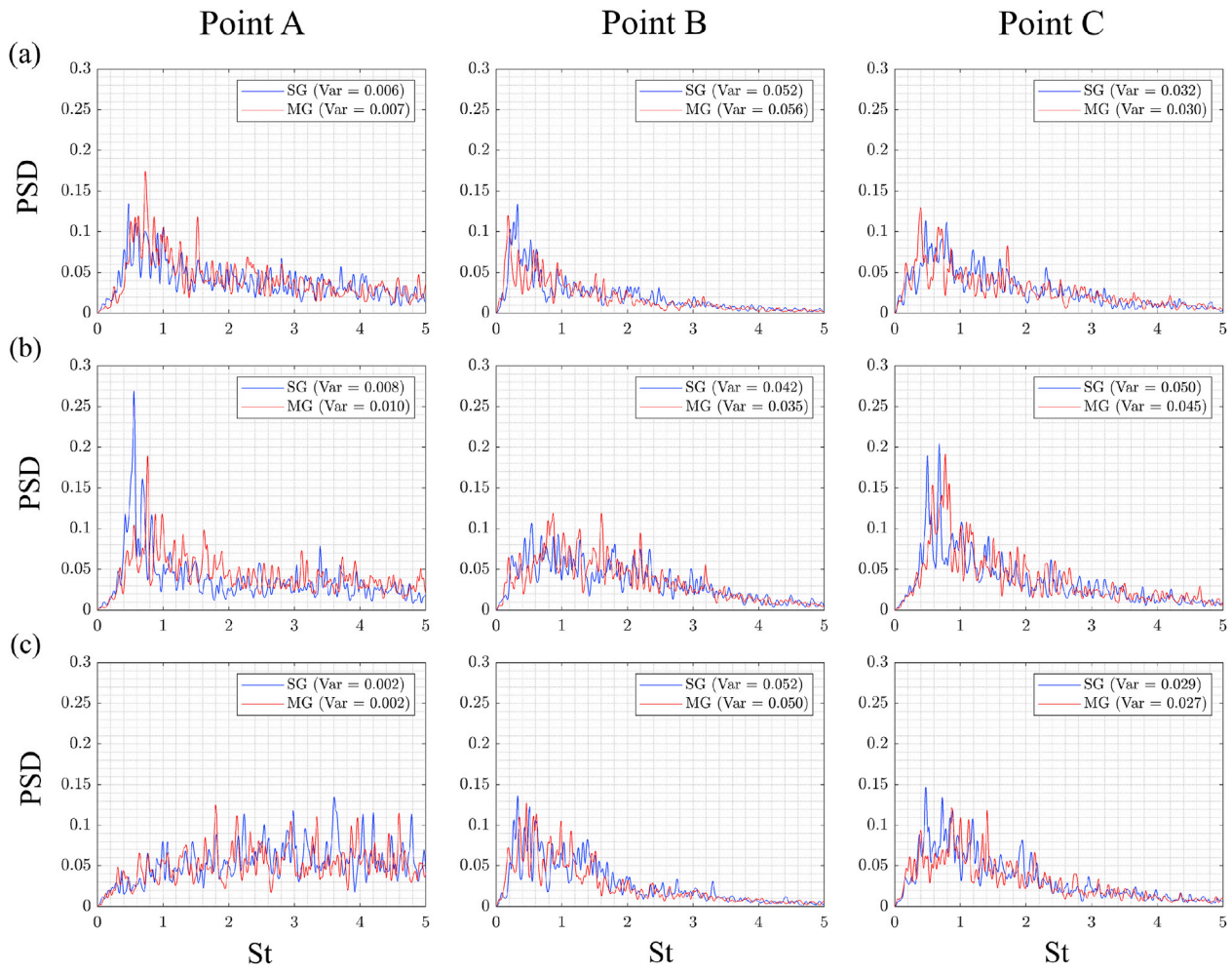

Fig. 11. The comparison of wake frequency based on St_A at the point A, B and C: (a) u; (b) v; (c) w, where the locations of the points are illustrated in Fig. 6.

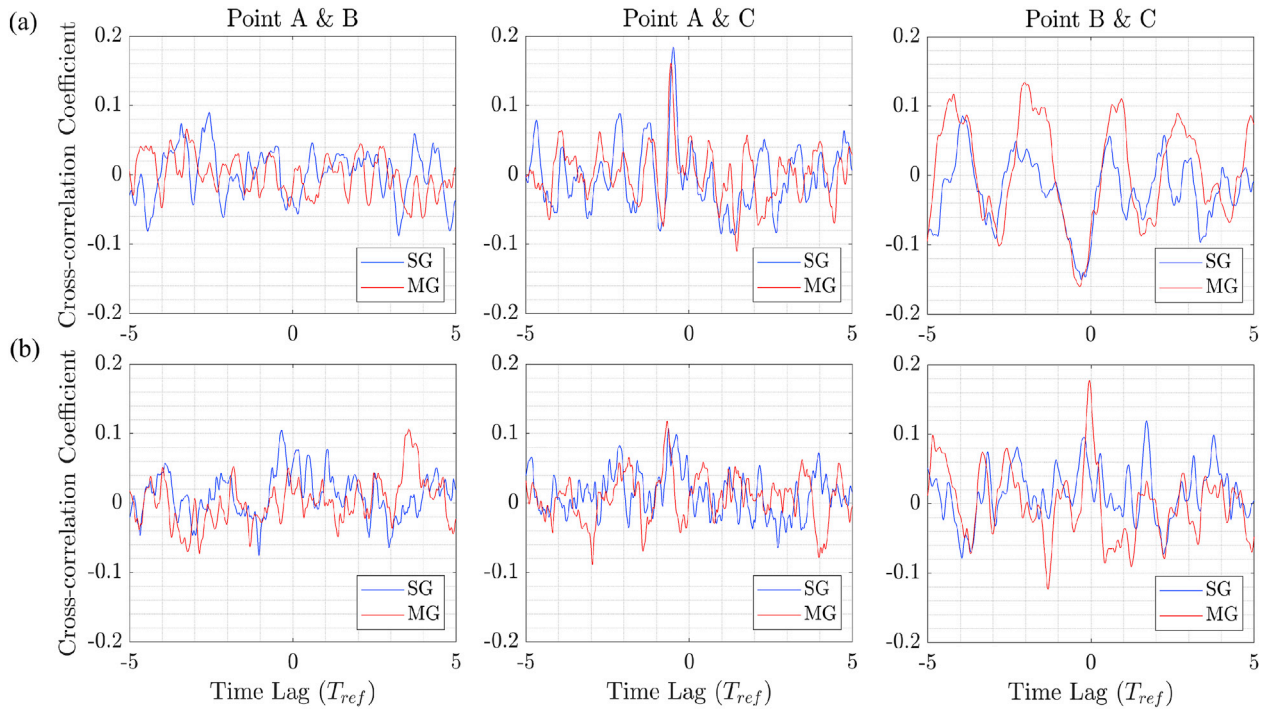

Fig. 12. The cross-correlation between the velocity data at point A, B and C: (a) *u*, (b) *w*, where the locations of the points are illustrated in Fig. 6.

The transient characteristics of the twin vortices are investigated based on the dynamic responses at the vortex cores, and cross-correlation between the left and right cores. As the core location is approximately the same for both cases, for consistency this study utilises the same core location at $x/H = 1$ with coordinates (*y*-coordinate, *z*-coordinate) of ($-0.2H$, $0.6H$), ($0.2H$, $0.6H$), as illustrated by the green "+" in Fig. 9(b). The frequency response of the vortex cores is represented by the power spectra of the velocity components at the left core ($-0.2H$, $0.6H$) as plotted in Fig. 13(a). Similar to Fig. 11, the core velocity signals show a wide range of frequencies with no distinct difference between the SG and MG cases. Additionally, Fig. 13(b) shows that no clear correlation can be identified from any velocity components. This implies that the interaction between the vortex pair is not dominant; two reasons may contribute. First, the strength of these vortices is low compared with the background level. For example, the strength of this vortex pair is significantly weaker than the one found behind a generic high-speed train (Wang et al., Thompson). Second, as shown in Fig. 9, the spin angle of the vortex cores indicate that the vortices tend to move away from each other, instead of pushing each other towards the centreplane, as determined in the rear pillar vortices or the longitudinal vortices behind a high-speed train.

Furthermore, Proper Orthogonal Decomposition (POD) is used to resolve the detailed makeup of most-energetic transient wake structures. POD is a widely used technique to extract coherent dynamic features from a turbulent flow field, by calculating the optimal orthogonal basis (modes) of fluctuations. This study employs the snapshot POD method, which was initially proposed by Sirovich, (1987), and has been extensively used to investigate the wake flows. In this study, POD is conducted based on the vorticity components (i.e., ω_x, ω_y and ω_z) at $x/H = 1$, and the structure of the two most energetic modes are presented in Fig. 14, with the corresponding energy percentage (E) listed. Clearly, these energy percentages are low but consistent with the broad spectra examined previously. This is indicative of the chaotic nature of the near wake. The sign of the mode in Fig. 14 is arbitrary, so that the mode 2 of ω_z are essentially the same mode. For the longitudinal vorticity component (ω_x), both SG and MG show a high energy fluctuation concentrated at the location of vortex cores as previously indicated in Fig. 9, but no clear mode structures can be concluded. The first mode of ω_y indicates a vertical energy fluctuation which is corresponding to the vertical oscillation of the shedding from the spoiler. The second mode of ω_y in SG represents a vertical energy alternation at the mid-height, which is imposed on the longitudinal vortices. In comparison, the second mode of ω_y in SG shows some loss of centreplane symmetry, suggestive that the length of the dataset to extract the POD modes is insufficient. However, given the limitation imposed by computational expense, it was difficult to justify an increased sampling time to better resolve the mode, especially for a chaotic flow field with no clearly dominant flow structures. Despite the issue of sub optimal convergence, the mode structure potentially indicates a diagonal and vertical energy fluctuation. High energy fluctuation regions for ω_z is concentrated at a lower height above the diffuser. The comparison between the SG and MG cases shows that the mode structures are consistent. For example, the first mode represents a pulsing at the centreline, while the second mode indicates a left/right oscillation.

3.2. Car surface pressure and aerodynamic loading

In this section, the car surface pressure distributions with the different ground motion conditions are compared, focusing on the base and underbody surfaces which are more sensitive to ground conditions. The pressure coefficient profile at the centreplane is then plotted for a quantitative comparison, and experimental data is provided for validation. Finally, the influence on the aerodynamic force components is presented.

To begin, the aerodynamic loading on the car surface is quantified through pressure coefficient (C_P) contours. For validation purposes, this study adopts the same formula for C_P as used in the wind-tunnel experiments (Avadiar et al., 2018), which is defined by

$$C_P = \frac{P_{sampled} - P_{ambient}}{P_{stagnation,front}}. \quad (1)$$

Here, $P_{sampled}$ is the local ambient pressure, and $P_{stagnation,front}$ represents the stagnation pressure at the front of the vehicle. The reference value $P_{ambient}$ is used to correct the local ambient pressure gradient in the wind-

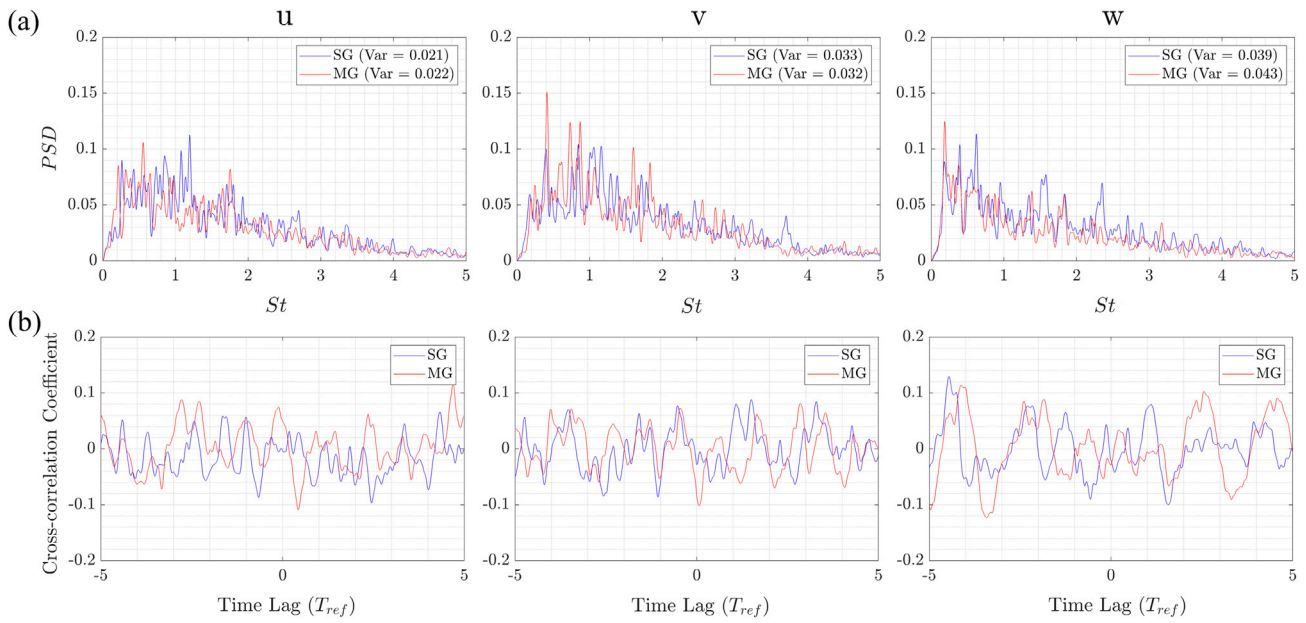

Fig. 13. The dynamic characteristics of the vortex cores: (a): power spectra of the velocity components; (b): cross-correlation of the velocity signals between the left and right cores.

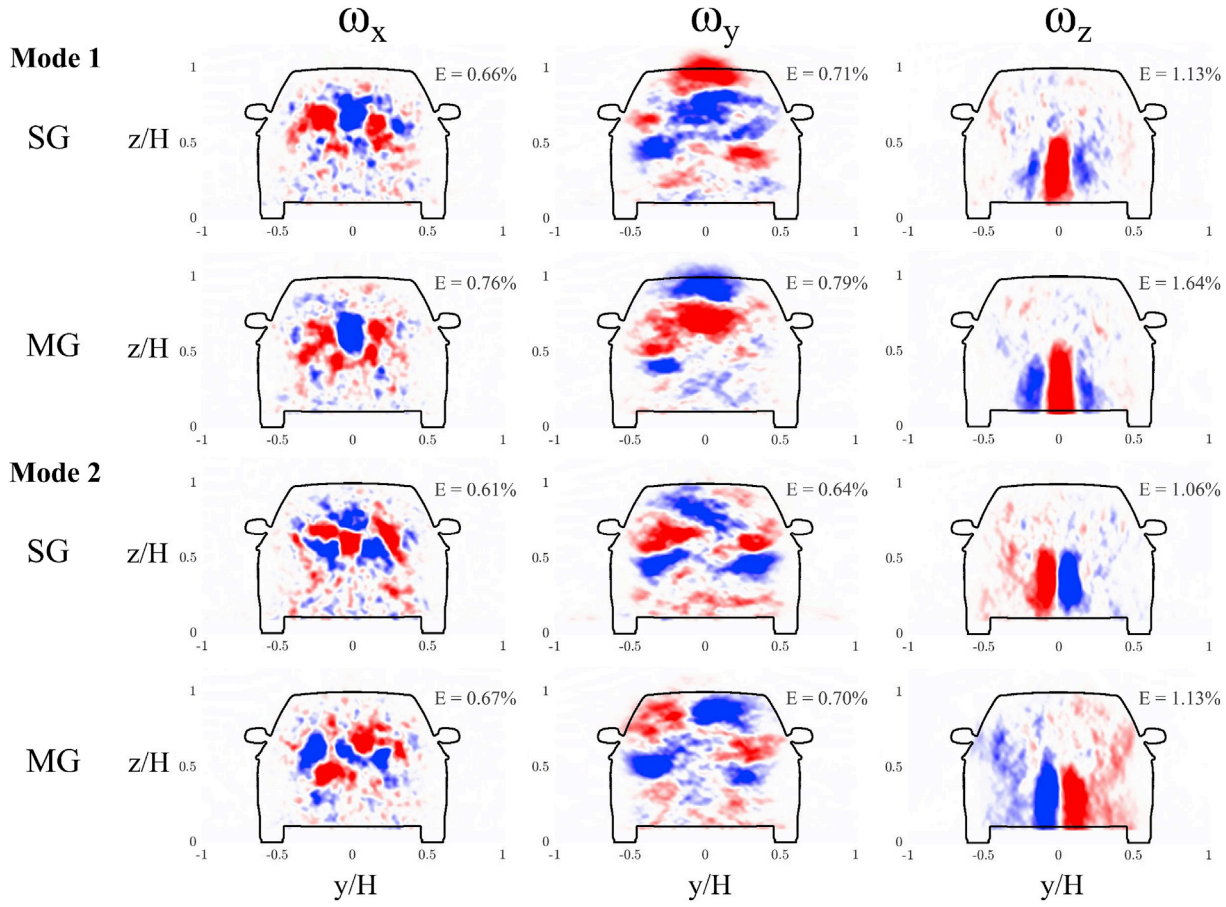

Fig. 14. The POD modes of x-, y-, z-vorticity at $x/H = 1$. For location referencing, the boundary of the car is plotted with a black solid line.

tunnel, but in this study it is set to zero. For the collaborative wind tunnel experiment, the pressure has been corrected for the pressure gradient due to blockage effect. A ratio of the static pressure from the base of the vehicle to the nozzle is measured in the empty wind tunnel at the same dynamic pressure as vehicle-present experiments. With the vehicle present, the nozzle static pressure, which had increased (within 1% of dynamic pressure) was applied as the reference P static. More details regarding the experimental testings can refer to (Avadiar et al., 2018).

The time-averaged base pressure distribution and corresponding standard deviation are presented in Fig. 15. The first two rows show the base pressure for the SG and MG cases, respectively, and the third row highlights the deviation between the two cases by calculating the absolute difference (i.e., MG-SG). According to Fig. 15, the difference between the SG and MG cases is negligible, except for the underbody and wheel regions. The pair of low pressure regions at the half vehicle height is expected due to the impingement of the wake vortices as described in Fig. 5. The high unsteadiness occurs around the wheels, side mirrors and the edge around the car base surface due to flow separation.

The pressure distribution on the underbody surface is then explicitly compared in Fig. 16. Similarly, the SG and MG results are presented in the first two rows respectively, and the absolute deviation between the cases (MG-SG) is highlighted in the third row. According to Fig. 16 (a) and (b), the underbody surface pressure contours are qualitatively consistent. Quantitatively, due to a higher flow flux with the moving ground, a higher pressure deviation is determined on the under-body structures, and wheel rotation introduces extra pressure deviation around the wheel housings.

Furthermore, the centreline pressure profiles are plotted in Fig. 17 with experimental measurements provided for validation, and good agreement is established between the CFD (SG case) and WT results. Not surprisingly, the SG and MG profiles are almost identical especially on the top surface. The entire part on the bottom is immersed in the negative pressure region, with the stationary ground slightly reducing its magnitude. Additionally, this effect is in line with experimental results from a study undertaken at Tongji university (Avadiar et al., 2018), which obtained wind tunnel results for the two ground configurations.

Finally, the ultimate impact of the two ground configurations on the integral aerodynamic force is presented. Both the drag (C_D) and lift (C_L) coefficients are calculated from the surface pressure and shear stress, and the results are listed in Table 3. As shown in the surface pressure distribution, the alteration due to ground motion is mainly determined by the

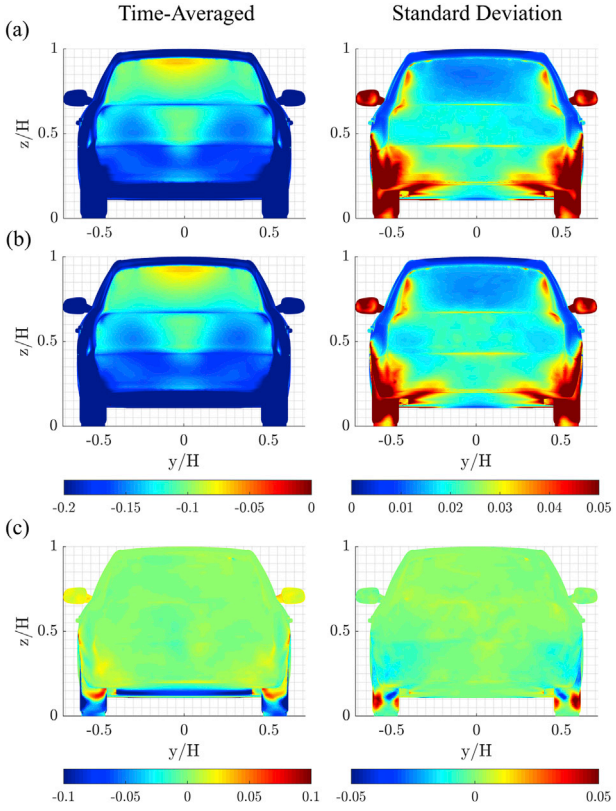

Fig. 15. The comparison of time-averaged base pressure coefficient and corresponding standard deviation: (a) SG; (b) MG; (c) MG-SG.

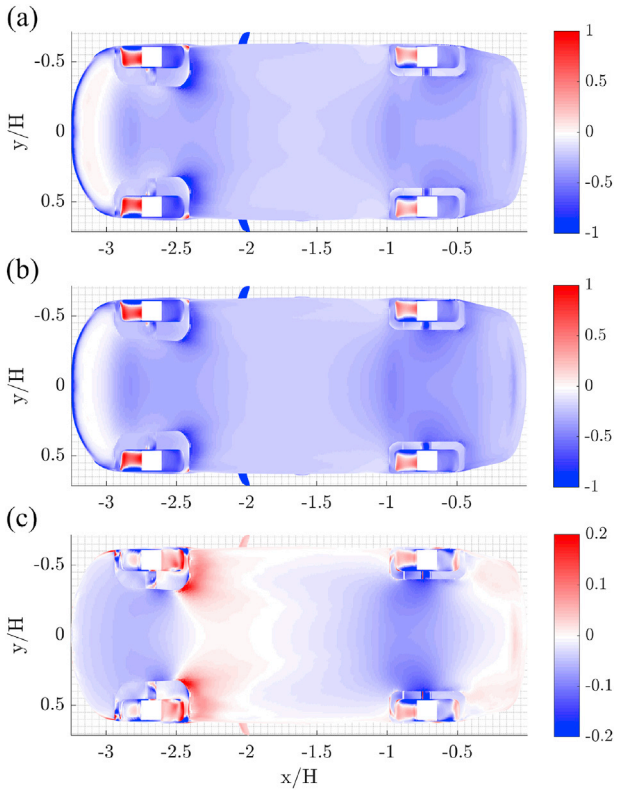

Fig. 16. The comparison of underbody pressure coefficient: (a) SG; (b) MG; (c) MG-SG.

underbody surface. Therefore, the ground motion effect is more significant on the vertical loading (C_L) comparing to that in the streamwise direction (C_D), while the standard deviations for both directions are relatively insensitive to the ground configuration. Additionally, the C_D value predicted by this study is compared with the other studies on the same car, as presented in Table 4. The drag prediction from this study is consistent with the previous studies, which together suggest that the impact of ground configuration on drag is less profound compared with that seen for the DriAver-Fastback and -Notchback (Heft et al., 2012b). Specifically, for the current study, the two predictions are within 3% of each other (0.307–SG: 0.298–MG). Note that this difference is well within the range of drag measurements from different wind-tunnel studies for the stationary ground configuration. The force presented in Table 3 include both the wheels and body components. Please note that in Table 4, both Heft et al. (2012b) and Collin et al. (2016) measured the drag of the main car body on a single-belt system with the wheels being isolated and rotated by four struts. On the other hand, the lift coefficient varies between the two cases by approximately a factor of two. Compared to drag, the lift is more difficult to accurately measure, and is sensitive to the flow conditions. Therefore, its value has been less reported in the literature. Collin et al. (2016) reported the lift coefficient obtained from two wind tunnels, the Technical University of Munich and at Audi, and the results were −0.154 and −0.131, respectively. Please note that, moving belts were used to obtain the measurements, while the wheel lift was not included. In the same study, a numerical simulation with a free-slip ground condition predicted a lift coefficient of −0.205 (Collin et al., 2016).

To complete the investigation, an extra case with half the ground clearance was modelled. This was motivated by the accepted view that race cars with small ground clearance require a moving ground for accurate force predictions. The modifications here are that the wheels are moved up by 83.5 mm (to reduce the ground clearance by a factor of two), with the inside surface of the wheel housing trimmed to accommodate this. All other features remain identical, for example, the exterior

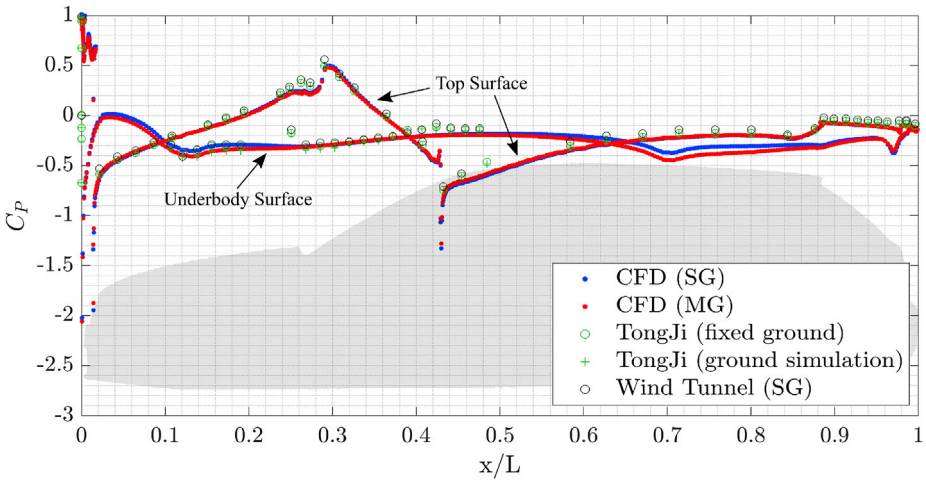

Fig. 17. The comparison of the centreline pressure coefficient profiles. The shaded vehicle shape is for location referencing purposes. The Tongji data is provided with the courtesy of Ford Motor Company.

Table 4
The comparison of aerodynamic loadings between the SG and MG cases.

Study	C_D	Re ($\times 10^6$)	Ground configuration
SG (current study)	0.307	8	Fixed
wind-tunnel (collaborative study) (Avadiar et al., 2018)	0.291	8	Fixed
Heft et al. (2012b)	0.296	5.2	Fixed
Ashton and Revell, (2015)	0.306–0.313	4.9	Fixed
MG (current study)	0.298	8	Ground simulated
Heft et al. (2012b)	0.292	5.2	Ground simulated
Collin et al. (2016)	0.295	11	Ground simulated
Collin et al. (2016)	0.298	5.2	Ground simulated

car geometry remains unchanged. Due to the high cost of DES simulations, 50 KCPU hours per case in this study, the half ground clearance cases are resolved by RANS simulations. The computed C_Ds of the stationary and moving ground cases were 0.253 and 0.254, respectively. Note that the equivalent RANS predictions for the drag of the normal ground clearance cases were 0.279 (SG) and 0.262 (MG), consistent with the more expensive IDDES simulations. These additional simulations show that for the DrivAer-Estate, the value of C_D is sensitive to the ground clearance, but again the effect due to differences in ground motion is minimal. Of course, more detailed and accurate analysis of the ground motion effect at a lower ground clearance height could be achieved by scale-resolving simulations (e.g., DES).

4. Conclusions

In conclusion, in this paper both time-averaged and dynamic flow characteristics around a generic estate vehicle (DrivAer-Estate), together with the corresponding aerodynamic loadings, subject to two different ground configurations, have been thoroughly investigated. Primarily, this study shows that the flow field around, and in the wake of, a generic estate vehicle has the following distinct aerodynamic features compared with sedan or fast-back vehicles. First, the coherent time-averaged streamwise vortex pair that forms within the wake still exists but is not caused by the rear pillar vortices peeling off from the car surface and tilting downstream. Instead, it is formed from the interaction and merging of multi-scale near-wake structures and realignment of near-wake vorticity into the downstream direction. In this case, the presence of the vortex pair is only clear some distance from the rear of the vehicle. In addition, the overall strength of the counter-rotating pair is weaker than for the fast-back wake. Second, there is no significant indication of downwash present within the wake, leading the vortex pair to propagate almost horizontally downstream. Of course, self-induction of the vortex pair should also propagate the pair towards the ground as it moves downstream, so this is also an indication of the relatively weaker strength of the pair. Dynamically, the broad power spectra of wake velocity components and lack of strongly dominant (energetic) proper orthogonal decomposition modes indicate that the wake is very chaotic, suggesting that it consists of multiple smaller-scale geometry-generated and turbulent features instead of being dominated by more energetic quasi-periodic dynamic features, such as identified for other vehicle types. By comparing the flow characteristics with stationary or moving ground, the results show that the impact of ground motion is exerted through the ground boundary layer growth, and it only alters the flow field in proximity to the ground. However, as the main wake features, such as the formation and propagation of the trailing vortical structures, locate beyond the ground boundary layer region, the impact of the ground configuration on the flow characteristics around the DrivAer-Estate is limited. In line with the limited influence on the wake-flow structure, the identifiable effect on the surface pressure due to the ground configuration is only apparent on the underbody surface. Consequently, the ground boundary condition only has a significant impact on the lift prediction, changing it by a factor of approximately two, but its influence on the drag is minimal, with the time-mean predictions within 3% of each other. This work has specifically investigated the wake flow structures, base pressure distribution and wake velocity provided proposals to account for the differences to the flow topology. Many other studies do examine the body forces, and examine the general wake topology without providing more detail. However, the underlying reason why the ground condition on an estate-type vehicle has limited influence remains undetermined. The present study tries to answer this question by determining the effects of ground motion on the flow features around the vehicle, and hence improve the current understanding of why such a vehicle type is relatively less sensitive to ground motion. This study additionally provides examples of methodology that can be applied to further analyse results for numerical work that investigate testing facility configurations, with most numerical studies utilising an unsteady solver. Further detailed wake information on the full-scale DrivAer-Estate is provided, providing greater fidelity than might be feasible in experiments. The long solve time for the transient simulation has shown the energy content of the wake's vorticity to have little coherence or clear oscillatory behaviour, as shown by the POD results.

References

Ahmed, S.R., Ramm, G., Faltin, G., 1984. Some salient features of the time-averaged ground vehicle wake. SAE Trans. 473–503.

Aljure, D., Lehmkuhl, O., Rodriguez, I., Oliva, A., 2014. Flow and turbulent structures around simplified car models. Comput. Fluid 96 (3), 122–135.

Ashton, N., Revell, A., 2015. Comparison of rans and des methods for the drivaer automotive body, Tech. rep. SAE Technical Paper.

Avadiar, T., Thompson, M., Sheridan, J., Burton, D., 2018. Characterisation of the wake of the drivaer estate vehicle. J. Wind Eng. Ind. Aerodyn. 177, 242–259.

Avadiar, T., Thompson, M., Sheridan, J., Burton, D., 2019. The influence of reduced Reynolds number on the wake of the drivaer estate vehicle. J. Wind Eng. Ind. Aerodyn. 188, 1–10.

Bearman, P., De Beer, D., Hamidy, E., Harvey, J., 1988. The Effect of a Moving Floor on Wind-Tunnel Simulation of Road Vehicles, Tech. Rep. SAE Technical Paper.

Bonnavion, G., Cadot, O., Evrard, A., Herbert, V., Parpais, S., Vigneron, R., Délery, J., 2017. On multistabilities of real car's wake. J. Wind Eng. Ind. Aerodyn. 164, 22–33.

Brewer, P.F., 2017. Record Year for Motor Industry in.

Cogotti, A., 1998. A Parametric Study on the Ground Effect of a Simplified Car Model. Report.

Collin, C., Mack, S., Indinger, T., Mueller, J., 2016. A numerical and experimental evaluation of open jet wind tunnel interferences using the drivaer reference model. SAE International Journal of Passenger Cars-Mechanical Systems 9, 657–679, 2016-01-1597.

Drivaer model, https://www.aer.mw.tum.de/en/research-groups/automotive/drivaer/, accessed: 2018-09-26..

Duell, E.G., George, A., 2000. Experimental Study of a Ground Vehicle Body Unsteady Near Wake. SAE International.

Duncan, B.D., Kandasamy, S., Sbeih, K., Lounsberry, T.H., Gleason, M.E., 2010. Further Cfd Studies for Detailed Tires Using Aerodynamics Simulation with Rolling Road Conditions, Tech. Rep. SAE Technical Paper.

A. Fluent, 12.0 Theory Guide, Ansys Inc vol. 5 (5).

Graftieaux, L., Michard, M., Grosjean, N., 2001. Combining piv, pod and vortex identification algorithms for the study of unsteady turbulent swirling flows. Meas. Sci. Technol. 12 (9), 1422.

Grandemange, M., Gohlke, M., Parezanović, V., Cadot, O., 2012. On experimental sensitivity analysis of the turbulent wake from an axisymmetric blunt trailing edge. Phys. Fluids 24 (3), 035106. https://doi.org/10.1063/1.3694765.

Grandemange, M., Cadot, O., herbert, C.A.v., Ricot, D., Ruiz, T., Vigneron, R., 2015. A study of wake effects on the drag of the ahmed's squareback model at the industrial scale. J. Wind Eng. Ind. Aerodyn. 145, 282–291. https://hal-ensta.archives-ouvertes.fr/hal-01205907.

Guilmineau, E., 2014. Numerical simulations of ground simulation for a realistic generic car model. In: ASME 2014 4th Joint US-European Fluids Engineering Division Summer Meeting Collocated with the ASME 2014 12th International Conference on Nanochannels, Microchannels, and Minichannels. American Society of Mechanical Engineers. V01CT17A001–V01CT17A001.

Guilmineau, E., 2014. Numerical simulations of flow around a realistic generic car model. SAE International Journal of Passenger Cars-Mechanical Systems 7, 646–653, 2014-01-0607.

Heft, A., Indinger, T., Adams, N., 2011. Investigation of unsteady flow structures in the wake of a realistic generic car model. In: 29th AIAA Applied Aerodynamics Conference, p. 3669.

Heft, A.I., Indinger, T., Adams, N.A., 2012. Experimental and numerical investigation of the drivaer model. In: ASME 2012 Fluids Engineering Division Summer Meeting Collocated with the ASME 2012 Heat Transfer Summer Conference and the ASME 2012 10th International Conference on Nanochannels, Microchannels, and Minichannels. American Society of Mechanical Engineers, pp. 41–51.

Heft, A.I., Indinger, T., Adams, N.A., 2012. Introduction of a New Realistic Generic Car Model for Aerodynamic Investigations. Tech. Rep.. SAE Technical Paper.

Hennig, A., Widdecke, N., Kuthada, T., Wiedemann, J., 2011. Numerical comparison of rolling road systems. SAE International Journal of Engines 4, 2659–2670, 2011-37-0017.

Howell, J., Hickman, D., 1997. The Influence of Ground Simulation on the Aerodynamics of a Simple Car Model. Tech. Rep.. SAE Technical Paper.

Krajnović, S., Davidson, L., 2005. Influence of floor motions in wind tunnels on the aerodynamics of road vehicles. J. Wind Eng. Ind. Aerodyn. 93 (9), 677–696.

Le Good, G.M., Garry, K.P., 2004. On the Use of Reference Models in Automotive Aerodynamics. Tech. Rep.. SAE Technical Paper.

Littlewood, R., Passmore, M., Wood, D., 2011. An investigation into the wake structure of square back vehicles and the effect of structure modification on resultant vehicle forces. SAE Technical Journal of Engines 4 (2), 29–37.

Pavia, G., Passmore, M., Sardu, C., 2018. Evolution of the bi-stable wake of a square-back automotive shape. Exp. Fluid 59 (1), 20.

Sirovich, L., 1987. Turbulence and the dynamics of coherent structures. i. coherent structures. Q. Appl. Math. 45 (3), 561–571.

Soares, R.F., Garry, K.P., Holt, J., 2017. Comparison of the Far-Field Aerodynamic Wake Development for Three Drivaer Model Configurations Using a Cost-Effective Rans Simulation. Tech. Rep.. SAE Technical Paper.

Volpe, R., Devinant, P., Kourta, A., 2014. Unsteady Experimental Characterization of the Natural Wake of a Squareback Ahmed Model. ASME.

Wang, S., Burton, D., Herbst, A.H., Sheridan, J., Thompson, M.C., 2018. The effect of the ground condition on high-speed train slipstream. J. Wind Eng. Ind. Aerodyn. 172, 230–243.

S. Wang, D. Burton, A. H. Herbst, J. Sheridan, M. C. Thompson, The effect of bogies on high-speed train slipstream and wake, J. Fluids Struct. 83.

Worldwide Harmonized Light Vehicles Test Procedure (WLTP).

Zhang, X., Toet, W., Zerihan, J., 2006. Ground effect aerodynamics of race cars. Appl. Mech. Rev. 59 (1), 33–49.